Journal of Earth Science, *Vol. 27*, *No. 6*, *p. 955–970*, *December 2016* *ISSN 1674-487X*
Printed in China
DOI: 10.1007/s12583-015-0656-2

Tertiary and Quaternary Marine Terraces and Planation Surfaces of Northern Oman: Interaction of Flexural Bulge Migration Associated with the Arabian-Eurasian Collision and Eustatic Sea Level Changes

Ye Yuan[1], **Timothy M. Kusky***[1, 2], **Sankaran Rajendran**[2, 3]

1. *State Key Laboratory for Geological Processes and Mineral Resources*, *Three Gorges Research Center for Geohazards*, *Ministry of Education*, *China University of Geosciences*, *Wuhan* 430074, *China*
2. *Center for Global Tectonics*, *School of Earth Sciences*, *China University of Geosciences*, *Wuhan* 430074, *China*
3. *Department of Earth Sciences*, *Sultan Qaboos University*, *Al-Khod*, *Muscat* 123, *Oman*

ABSTRACT: The northeastern Arabian passive margin is being subducted beneath the Zagros and Makran of Iran. A flexural bulge related to the weight of the Makran has migrated at 4 cm/a through the previously uplifted Hajar Mountains of Oman as this active convergence and collision between Arabia and Eurasia progresses, adding approximately another 500 meters of relief, and forming a series of uplifted marine terraces, alluvial terraces, and planation surfaces that record the passage of the bulge. We use a combination of field studies, remote sensing and GIS to map and better-understand these terraces, and elucidate how the tectonics of bulge migration, down-to-trench normal faulting, and eustatic sea level changes have interacted to produce the extant geomorphic features on the inner slope of the flexural bulge as it sinks into the foredeep of the Gulf of Oman. We speculate those terraces that were uplifted on the outer slope of the forebulge as it initially migrated through the passive margin (affected by ophiolite obduction in the Cretaceous) 3.75–7.5 Ma ago are now sinking on the inner slope of the forebulge (corresponding to the outer trench slope in the foredeep), and have been partly covered by Quaternary marine terraces related to a Weichselian sea level high stand. Both the Tertiary and Quaternary terraces are cut by faults related to the active collision, confirming that there is a significant risk of moderate earthquakes in the region.

KEY WORDS: marine terraces, flexural bulge, Arabia-Eurasia collision, Sultanate of Oman, remote sensing, image processing, Quaternary sea level fluctuation.

0 INTRODUCTION AND PREVIOUS RESEARCH

The Hajar Mountains of Oman and the United Arab Emirates (UAE) are located on a promontory on the NE margin of the Arabian Plate (Fig. 1), bounded to the SW by spreading ridges in the Red Sea and Gulf of Aden. Its east and west boundaries are delineated by transform faults, the Owen fracture zone to the east and the Dead Sea transform to the west. The northern margin is marked by the collision zone between the Arabian Plate and Eurasia where Arabian continental crust is being subducted beneath the Zagros fold belt of Iran, and oceanic crust of the Arabian Plate is being subducted beneath the Makran depression. The boundary between continental and oceanic subduction is marked by the Dibba line-Zendan fault-Oman line (Fig. 1). Present-day plate motions calculated from seafloor spreading rates and interplate fault motion poles for the relevant major plates demonstrate an increasing amount of plate convergence, from 35.5–36.5 mm/a in the west to 40–42 mm/a in the east (DeMets et al., 2010).

The Tiwi-Fins area lies on the northern flank of the Hajar Mountains, which form the foreland margin of the active collision zone between the passive margin of the Arabian Plate and the accretionary wedge of the Makran fold belt (Figs. 1–2). To the west of the Dibba line in Oman and the Zendan fault-Oman line in Iran, continental crust of the Arabian Plate is experiencing shallow subduction beneath the Zagros fold belt, whereas east of this line the Arabian Plate includes stretched continental crust and sea floor in the Gulf of Oman being subducted beneath the Makran (Glennie et al., 1990).

The tectonic history of this part of the Hajar Mountains is complex, and includes deposition of a Permian–Triassic carbonate platform along the southern margin of Tethys, parts of which are preserved in the Gulf of Oman (Mann et al., 1990). Collision of the northern Oman margin with a forearc in the Late Cretaceous terminated sedimentation on the margin, obducted the Samail ophiolite, and initiated subsidence and

*Corresponding author: tkusky@gmail.com
© The Authors 2016. This article is published with open access at Springerlink.com

Manuscript received January 7, 2016.
Manuscript accepted April 15, 2016.

Yuan, Y., Kusky, T. M., Rajendran, S., 2016. Tertiary and Quaternary Marine Terraces and Planation Surfaces of Northern Oman: Interaction of Flexural Bulge Migration Associated with the Arabian-Eurasian Collision and Eustatic Sea Level Changes. *Journal of Earth Science*, 27(6): 955–970. doi:10.1007/s12583-015-0656-2. http://en.earth-science.net

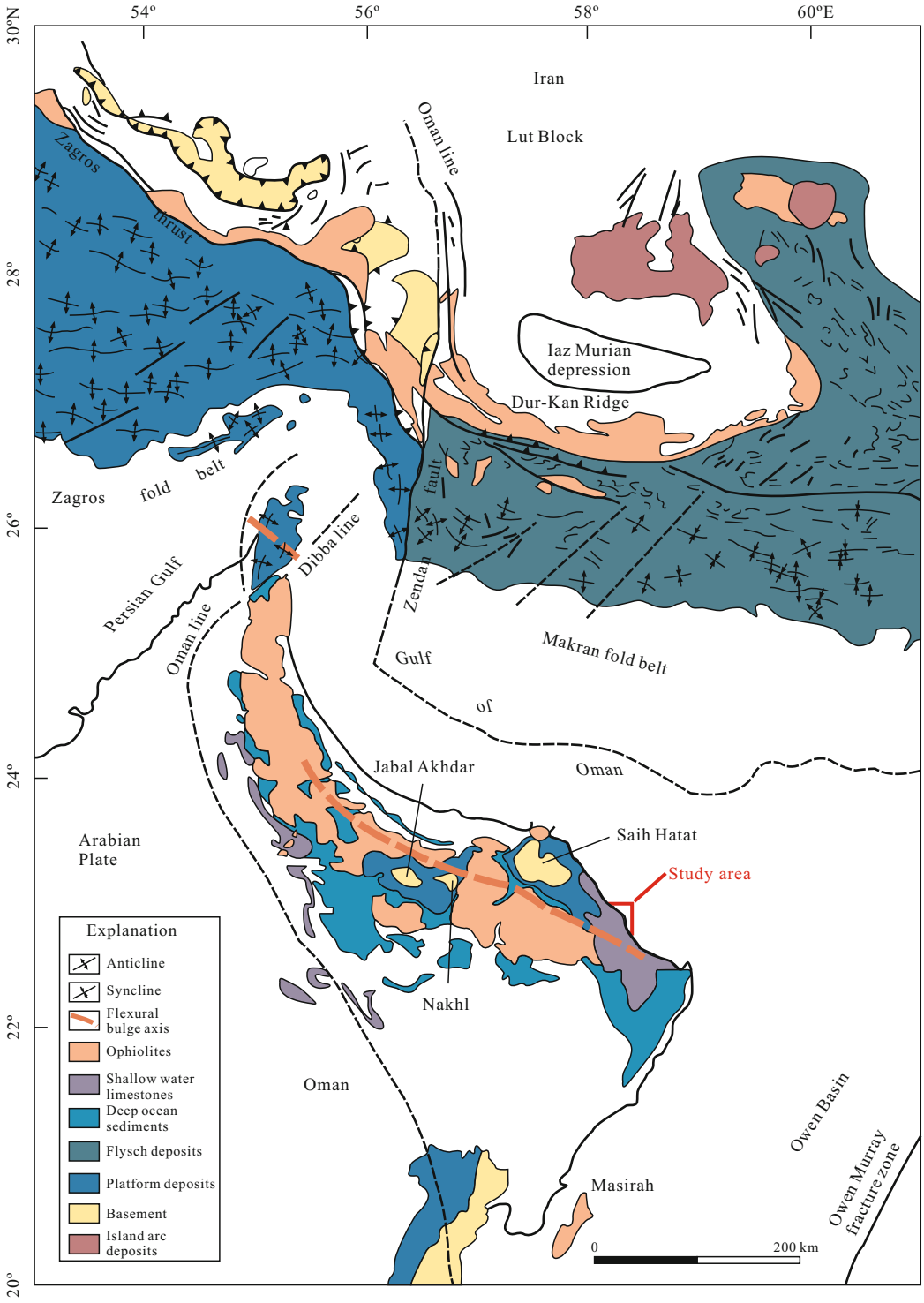

Figure 1. Map showing the tectonic setting of the northern Oman margin (modified after Kusky et al., 2005 and Boote et al., 1990).

sedimentation in the Aruma foreland basin (Rollinson et al., 2014); Glennie, 2005; Robertson, 1987; Glennie et al., 1973). Emplacement of the ophiolite caused strong deformation of the shelf sediments of the Hajar Group along with the oceanic and continental slope sediments of the Hawasinaa and Sumeini Groups and formed a thin dynamothermal aureole (Rollinson et al., 2014, and chapters therein). Large basement-cored antiformal domes at Jabal Akhdar, Nakhl, and Saih Hatat (Fig. 1) formed during this Late Cretaceous tectonism, either above basement ramps from deep duplexing, or propagation of blind thrusts (Rollinson et al., 2014; Al-Lazki et al., 2002; Hanna, 1986). This ophiolite-emplacement related deformation ended by the Late Campanian (Glennie, 2005) and was followed by Late Cretaceous–Early Tertiary shallow marine conditions.

It has long been a puzzle why the Hajar Mountains are still relatively high (locally above 3 000 m at Jabal Shams near Jabal Akhdar, Fig. 1), but the relief is clearly related to active tectonism (Kusky et al., 2005). Small to medium earthquakes occasionally shake the region (Deif et al., 2013). Convergence between the northern Oman margin and the Zagros-Makran

wedge was re-established by Eocene times (Mann et al., 1990). Tertiary structures in the central Hajar Mountains have been attributed to gravity tectonics (Glennie, 2005), down-to-basin normal faulting (Mann et al., 1990), or passage of a flexural bulge related to the Arabia-Eurasia collision (Kusky et al., 2005) as supported by gravity data (Ravaut et al., 1997). Kusky et al. (2005) were able to show from a comprehensive program of mapping late faults, drainage networks, topography, and terraces that Tertiary–Quaternary structures and geomorphic features are related to the contemporaneous subduction and imminent collision with the Makran to the north. They showed that the axis of current uplift is about 150 km south of the active thrust front of the Makran, and that systems of NW and WNW striking faults are contemporaneous outer trench slope normal faults, whereas a system of NNE-striking faults are probably tear faults separating different fault blocks sliding into the trench.

In this contribution we examine a series of marine terraces and planation surfaces in the Fins-Tiwi area identified by Kusky et al. (2005) who suggested that they may represent marine terraces uplifted on the outer flank of the flexural bulge that are now subsiding into the trench towards sea level on the outer trench slope (the inner flank of the flexural bulge). In this model the terraces closest to the shoreline should be the oldest since they were uplifted on the continental side of the forebulge, then as the bulge migrated through the foreland area of the Arabian Plate they would pass the bulge and start to sink back into the depths of the Gulf of Oman (Fig. 1). This simple scenario could be altered, however, by the effects of rising and falling sea-levels and the interaction between eustacy and tectonics (Fig. 1). We have used a combination of field data, remote sensing, and structural/stratigraphic analysis as a first step to test whether the terraces are related to tectonic uplift and subsidence on the forebulge, or to Tertiary–Quaternary sea level changes, or both.

1 FIELD STUDY

Figure 2 is a geological map of the Tiwi-Fins study area shown by the box in the center of the figure and its environs. In the SW rocks of the Samail ophiolite and Hawasina nappes are thrust over older shelf sequences of the Hamrat Duru Group and Hajar Supergroup derived from the Arabian Platform. In the NE these are overlain by Tertiary post-nappe units of the Fars, Dhofar, and Hadhramaut Groups. These are succeeded by Quaternary deposits that include marine terraces, slope colluvium, fans, and alluvial terraces, and giant sand dunes of the "Wahiba Sands" (Robinson et al., 2007). We have focused on the Tertiary and Quaternary sequences on the NE slope of Jabal Bani Jabir in the NE part of the area (Fig. 2).

Jabal Bani Jabir is comprised of a Tertiary limestone plateau separated from the Gulf of Oman by a narrow coastal plain. Elevations range from 1 700 m in the north to 2 223 m at Jabal Khadar in the south. The mountains are primarily composed of limestone overlain by Quaternary slope colluvium and scree deposits (Figs. 3–4). At Jabal Hulayyat on the coast, the mountains are built of Precambrian crystalline basement, composed of gneiss and mica schist intruded by granitic rocks (Wyns et al., 1992).

The Tertiary succession consists of a number of formations ascribed to three stratigraphic groups: the Hadhramaut, the Dhofar, and Fars Groups (Wyns et al., 1992). To the east the succession is relatively thin (200–300 m) and comprised of shelf limestones of the Seeb (Hadhramaut Group) and Shama (Dhofar Group) Formations. In central locations the Tertiary limestone is exceptionally thick (2 500–3 500 m) with a massive basal unit comprised of restricted shelf facies limestone of the Jafnayn Formation overlain by several formations belonging to the Hadhramaut Group and slope deposits from the Dhofar Group (Wyns et al., 1992). Thin deposits belonging to the Fars Group complete the succession. To the west, the Tertiary succession is made up of shelf deposits of the Hadhramaut Group, comprising the Jafnayn Formation (Late Paleocene–Early Eocene), the Rus Formation (Eocene), and the Seeb Formation (Wyns et al., 1992). Their total thicknesss in Jabal Bani Jabir measures between 1 200–1 500 m and decreases towards the west.

The Tertiary rocks are cut by several sets of faults (Fig. 2) including a prominent NW-striking set that parallels the mountain range and appears to accommodate differential uplift between different fault blocks. Other faults identified by Kusky et al. (2005) include an N-striking set and a NE-striking set that intersect near Tiwi (Fig. 2).

Figure 3 shows a detailed lithological map of the area around Fins-Ra's ash indicated by the box in Fig. 2, and displays the coastal deposits and terrace near Fins and Tiwi, and the older Tertiary deposits on Jabal Bani Jabir. The slopes of the mountain are dissected by a number of NW striking faults parallel to those in the present Arabia-Eurasia convergent zone in the Makran (Fig. 1). We have made detailed descriptions of the Tertiary and Quaternary strata, marine terraces, and older erosional surfaces in this area.

1.1 Tertiary

The Jafnayn Formation of the Hadhramaut Group in the study area (Fig. 3) consists of massive bioclastic limestone with subordinate conglomerate, sandstone and glauconitic marl (Wyns et al., 1992) forming series of limestone mesas. The sandstone and marl are interlayered with nodular and bioclastic limestone containing abundant algal debris and crushed fragments of benthic foraminifera, mainly alveolinids. The upper part of the limestone sequence is massive and forms a well-defined topographical surface above which a succession of alternating calcareous and clastic deposits overlap onto the Jafnayn Formation (Wyns et al., 1992).

The Abat Formation of the Hadhramaut Group (Fig. 3) consists of grey to white marly and micritic limestone with chert nodules, calciruditic and calcarenitic beds, and yellow glauconitic marl (Wyns et al., 1992). The formation is best exposed in wadis and broad depressions. The base of the Abat Formation is composed of dark-grey, thin-bedded lime mudstone with marl and partly silicified interbeds of laminated calcarenite. Trace fossils, flute-casts and slump structures occur in the lime mudstone which is interbedded with grey, thin-bedded limestone with marl in which slump structures are also common (Wyns et al., 1992). Minor resistant beds of calcirudite containing large blocks of reworked shelf carbonate are

present. A calcarenitic bed in the lower part preserves reworked benthic foraminifera that yield Paleocene to Eocene ages (Wyns et al., 1992).

The Rus Formation of the Hadhramaut Group outcrops at higher elevations in the SW part of the area (Fig. 3). It is a marine regressive unit deposited at the end of the Early Eocene (Ypresian) and consists of thin bedded dolomitic limestone and marl (Wyns et al., 1992). It is intercalated with the Jafnayn and Seeb formations and includes 80 m of gray micritic limestone interbedded with beige marl, forming depositional sequences one to several meters thick (Wyns et al., 1992). These deposits largely reflect a tidal flat environment with a few intervals interpreted as mangrove swamp deposits. It grades into the time-equivalent mudstone of the Abat Formation to the east (Wyns et al., 1992).

The Seeb Formation of the Hadhramaut Group consists of bioclastic limestone, calc-arenite, marl, and minor sandstone (Wyns et al., 1992) and is divided into two members, a lower Layh Member consisting of resistant limestone, and an upper unnamed member consisting of limestone, shale, and sandstone. It overlaps onto a hardground on the top of the Rus Formation, and caps the Jabal Bani Jabir mesa (Fig. 2).

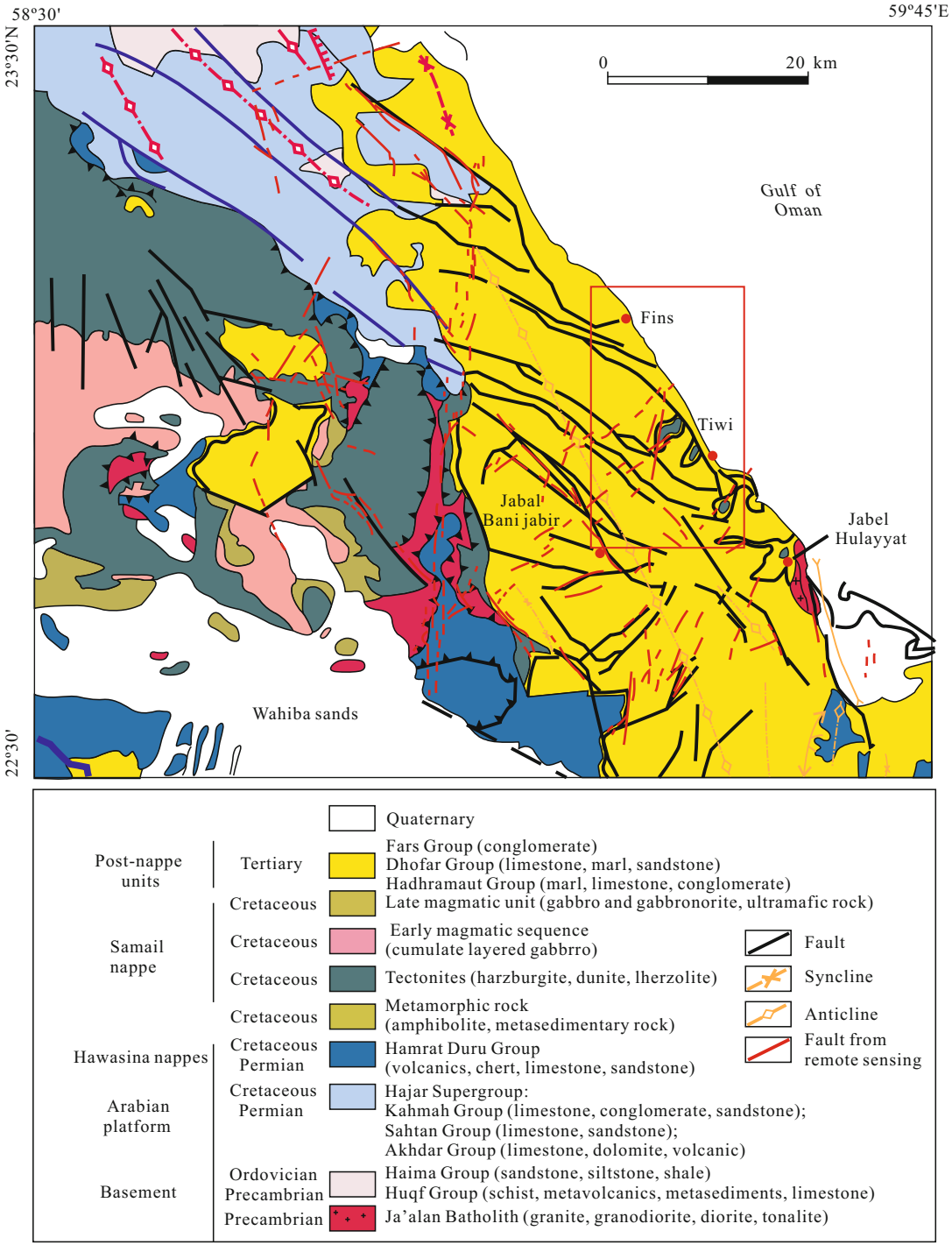

Figure 2. Geological map of the Tiwi area (modified after Kusky et al., 2005 and Wyns et al., 1992).

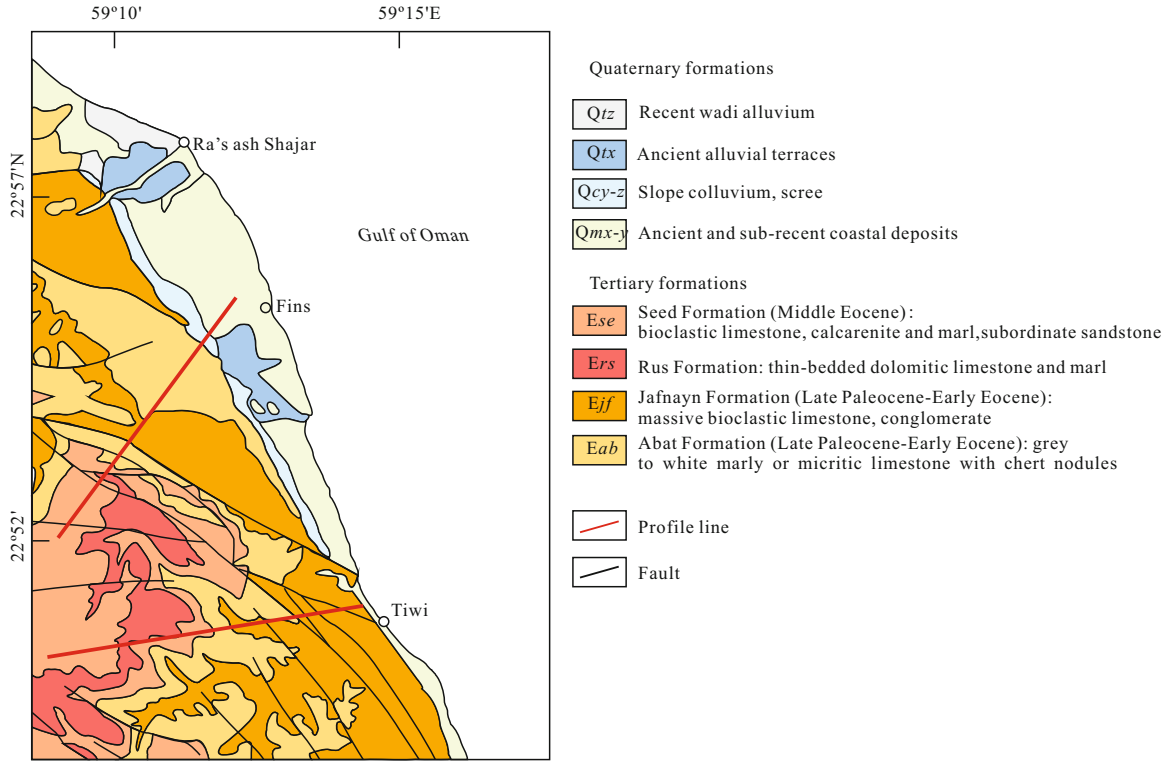

Figure 3. Detailed geological map of the area near Fins and Ra's ash Shajar (modified from Wyns et al., 1992).

In the map area in Wadi Tiwi (Fig. 3) the upper member of the Seeb Formation consists of 100 m of yellowish marl, succeeded by 150 m of poorly-consolidated quartz sandstone with plant impressions, laminated shale, and siltstone also with plant remains. This is followed by 250 m of yellow marl, clayey limestone, and calcirudite with quartz pebbles and nummulites capped by 150 m of resistant limestone forming the flat upper surface of the Jabal Bani Jabir mesa (Wyns et al., 1992).

1.2 Quaternary

Quaternary units include marine terraces, slope colluvium, scree, alluvial fans, and alluvial terraces (Fig. 3). Marine terraces occupy most of the coastal plain and were deposited at present elevations ranging between 50 and 10 m, with the highest between 25 and 50 m above the sea level (Wyns et al., 1992). Many of the terraces are covered by more recent deposits of slope colluvium and alluvium, and marine conglomerate (Figs. 4–5). The terraces are typically covered by rounded cobbles and boulders encrusted with oysters and some of the boulders are derived from an older marine conglomerate of Quaternary age. The thickness of the deposit increases towards the sea, whereas its grain size decreases in the same direction (Wyns et al., 1992).

The lower terraces, at altitudes of 10–20 m above sea-level, are particularly well developed on coastal plain between Fins and Tiwi (Figs. 3–5). Several meters of bound stone composed of coral and algae comprise the terrace surface (Wyns et al., 1992). The limestone is capped by several meters of marine conglomerate. Ancient barrier beach deposits with partly cemented pebbles are associated with these lower terraces. Slope deposits consisting of colluvium and scree form aprons at the foot of most of the cliffs formed of Tertiary strata. The deposits consist of poorly-sorted angular fragments that have fallen from the cliffs. Sliding and tilting of whole cliff-faces of limestone are linked to movements on the NW striking faults, some of which are listric and sole-out at the contact between the Tertiary units and the Hawasina nappes below (Kusky et al., 2005; Wyns et al., 1992).

Terrace IV is a composite terrace with multiple layers, that future detailed field work should be able to resolve. We present a preliminary description based on the resolution of our data. The lower elevation steps in Terrace IV (most at 10–20 and 30–50 m) are interpreted to reflect Quaternary sea-level fluctuations that varied between -100–120, and 22 m (Siddall et al., 2003; Chappell et al., 1996). Gardner (1988) dated mollusks from marine terraces 12–15 m above sea level in the Ra's al Jibsh area to be 21 280±280 years BP and 31 110±530 years BP. These data are consistent with data from drill cores in the port of Matrah near Muscat that show a sea-level high-stand at 17–20 m above present sea level at 31 890 years before present (Hannss et al., 1991). Thus we interpret the lower (10–20 m surfaces) of Terrace IV to be a result of a Quaternary sea level high during Weichselian times. The 30–50 m surfaces are older, but we are uncertain of their origin, and they require more detailed dating and geomorphic analysis.

Ancient alluvial fans and terraces are found at lower elevations than the older alluvial deposits, and form relatively extensive terraces. They are composed of pebbles to boulders, and are cemented with poorly sorted rolled clasts covered by thin dark oxidized coating.

Terraces occur at five main levels oriented WNW parallel to the coast and to the WNW striking set of faults (Figs. 2–3). At elevations of 10–20, 30–50 m (Type IV), 110, 140–150, and

180–200 m above sea level (Figs. 4–6). The Type IV terraces actually consist of a set of several different terraces mostly within the range of Quaternary sea changes. Types I, II, and III are planation surfaces higher than the range of Quaternary sea level rise. Type IV terrace deposits consist of a few meters of calcarenite matrix conglomerate containg *Pecten* and *Ostrea* shells deposited on old marine wave-cut platforms along with reworked Eocene foraminiferal microfauna (Wyns et al., 1992). Since the higher terraces are elevated well above the highest Pliocene–Quaternary eustatic sea-level highs (80 m at 4–5 Ma) the region demonstrably experienced considerable Pliocene–Quaternary uplift greater than 100 m (uplift minus maximum sea level rise). We attribute this uplift to the passage of the flexural bulge associated with the Arabian/Eurasian collision

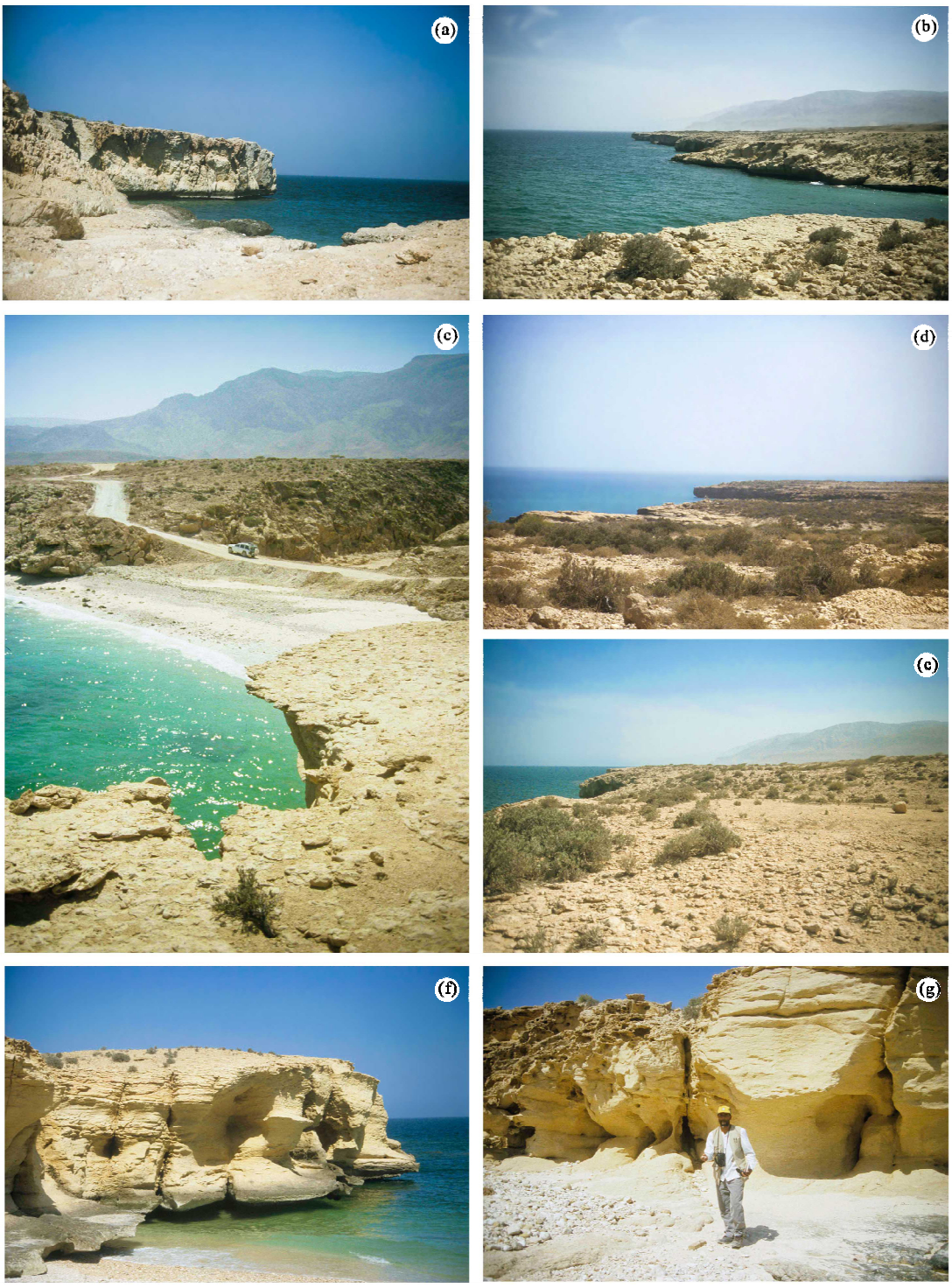

Figure 4. Field photographs showing Type IV marine terraces 10–20 and 30–50 m above sea level near Tiwi and Fins. (a)–(b) Gently seaward dipping marine terraces; (c) regional overview of a flat coastal terrace; (d)–(e) mollusk shell covered terrace; (f)–(g) Type IV terrace at Tiwi cut by NW and N-striking faults, demonstrating active Quaternary tectonism caused by the migrating flexural bulge.

Figure 5. Field photographs showing terraces and planation surfaces around Ra's ash Shajar and Fins region. (a) Composite Type IV marine terrace in the foreground stepping up to a Type I terrace; (b) gravel covered alluvial terrace with the Jabal Bani Jabir mesa in the background; (c) incised Type IV terrace with higher terraces behind.

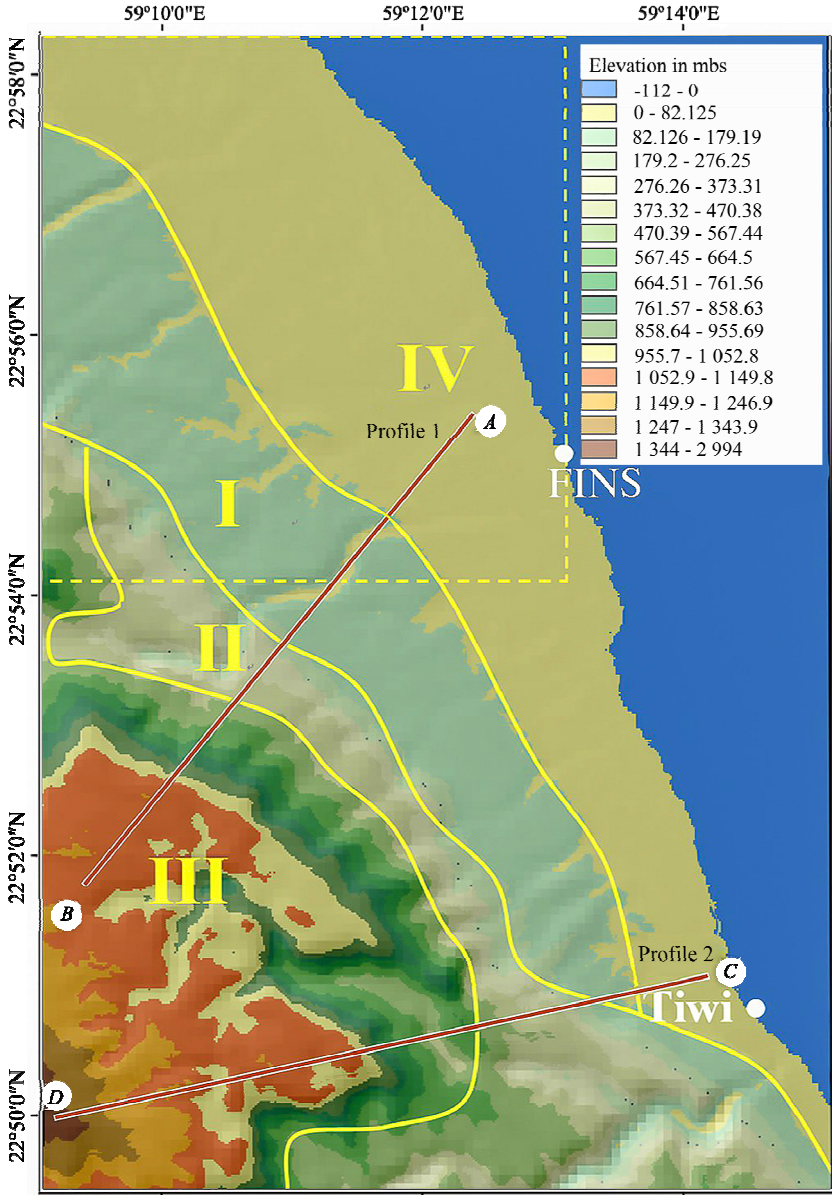

Figure 6. ASTER GDEM image of the Tiwi and Fins region showing types I, II, III and IV marine terraces. The dashed box is the region chosen for ASTER image analyses for the large scale study. Red lines *A–B* and *C–D* indicate the two profiles of cross-sections shown in Fig. 7.

(Fig. 3; Kusky et al., 2005) that caused differential motion on the WNW- and NNE-striking faults cutting the mountain front. In the next section we apply GIS and remote sensing techniques to identify and map these surfaces. In the following sections we provide a speculative model for the interaction of eustatic sea level changes and tectonic uplift associated with passage of the collision-related flexural bulge across the region.

2 METHODOLOGY

2.1 Remote Sensing Applications to Mapping Marine Terraces

Satellite images are powerful tools for mapping geomorphological features, lithology and structures of the Earth's surface using their distinct absorption characteristics. Studies were carried out using multispectral the remote sensing sensors such as Landsat, IRS, ASTER, SPOT, SRTM, InSAR for the identification and mapping of the terrace and planation surface features described above, following earlier pioneering work in these techniques (Li et al., 2015; Rajendran and Nasir, 2015, 2014; Van den Berg et al., 2015; Whitney and Hengesh, 2015; Zha et al., 2015; Haghipour and Burg, 2014; Li et al., 2012; Kusky et al., 2005; Kusky and Ramadan, 2002; Magilligan et al., 2002; Alsdorf and Smith, 1999; Williams et al., 1997; Richards, 1993). Haghipour and Burg (2014) used ASTER GDEM to analyze the coastal geomorphology and drainage system of the Makran accretionary wedge. Stollhofen et al. (2014) used satellite images to study the Pliocene–Pleistocene uplift of the Horingbaai delta fan, NW Namibia. This study uses ASTER, ASTER GDEM and Landsat ETM satellite data to map the marine terraces, planation surfaces, and their associated lithologies of the northern Oman passive margin as it begins to subduct beneath the Makran accretionary wedge. We pay particular attention to planation surfaces and marine terraces that may yield clues to the passage of the migrating flexural bulge as the Arabian Plate is bent under the load of the advancing Makran wedge.

2.2 Satellite Data and Methods

The seven multispectral bands of the Landsat ETM satellite data in the visible and reflected infrared regions, from 0.45 to 2.35 μm were used in this study with image interpretations integrated with ASTER GDEM data. The data were acquired on April 4, 2003 when there was 0% cloud cover over the selected study area. All images were initially resampled to a 30-m resolution and co-registered using topographic maps on the UTM projection coordinate system (Zone 40, Clarke 1980 spheroid, PSD93 datum with a root mean square error of less than 0.5 pixels per image) to identify ground control points. The data were preprocessed for geometric and radiometric corrections.

Details of the ASTER sensor are provided in Rajendran and Nasir (2015, 2014, 2013), Rajendran et al. (2013, 2012) and further explanation can be found in the ASTER user guide (http://asterweb.jpl.nasa.gov/content/03_data/04_Documents/aster_user_guide_v2.pdf). We should mention that the increased number of spectral bands in the SWIR region of ASTER (six compared with two for Landsat) provides more information about surface mineralogy and lithology for mapping. Fourteen ASTER Level 1B spectral bands were obtained for the study region on December 01, 2003 (AST_L1B_00312012003064653_20121127152917_4038) from NASA Land Processes Distributed Active Archive Center User Services, USGS Earth Resources Observation and Science (EROS) Center (https://LPDAAC.usgs.gov). The data for the study region were delivered in a tag image file (.TIF) format and consist of imagery and an ASCII text (.met) file of metadata. 0% cloud cover was confirmed, and the file checked for sensor errors such as banding and other geometric distortions. The data were supplied in the form of scaled radiance sensor data with radiometric and geometric corrections applied and georeferenced in the UTM projection for the WGS-84 ellipsoid. The nine VNIR-SWIR spectral bands were chosen and processed to map the limestone formations using ENVI (5) and ArcGIS (10) software. Mapping of terraces and the geology of the study region was carried out by decorrelation stretch, PCA and SAM image processing. The interpreted images were verified in the field and also using geological (Wyns et al., 1992) and traverse-based samples were collected for laboratory studies and geochronology. This work continues. Marine terrace levels in the study area were classified by interpretation of images at different scales and by the study of profiles of each terrace surface constructed from 2-m grid and 10-m grid digital elevation models (ASTER GDEMs) verified by field GPS data. Inner-edge elevations of the marine terrace surfaces were used to classify the terraces and determine the distribution of uplift.

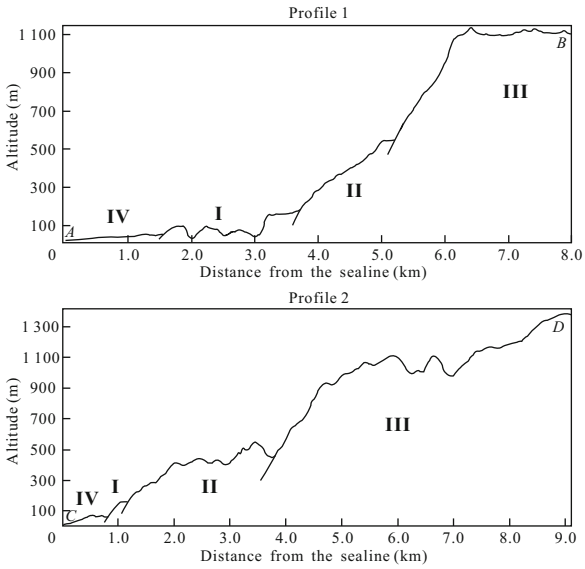

Figure 7. Topographic profiles along lines *A–B* and *C–D* with bold Roman numerals corresponding to terrace labels in Fig. 6. The terraces are bounded by faults of the NW striking set parallel to the Arabia-Eurasia collision zone in the Makran.

Terrace IV has a seaward-dipping surface actually composed of several sub-terraces at 10–20 and 30–50 m above sea level, which oversteps the older Terrace I. Terrace I is dissected and landward dipping. It is broken into two parts by a down-to-the-trench normal fault on profile 1 (Fig. 7). Terrace II is relatively narrow and bounded by normal faults, and has a steep associated scree slope. The surface of Terrace III forms a plateau over 1 km above sea level (Fig. 7) that is relatively flat in the area, and thus younger than surfaces I and II.

2.3 Image Analysis and Interpretations

A decorrelation stretching method was used to delineate the marine terraces of the Fins-Tiwi region. This method, based on a principal component transformation of the acquired data, is widely applied and has been discussed by Rajendran

and Nasir (2015, 2013), Philip et al. (2003), Matthews and Jones (1992), Abrams et al. (1988), Rothery (1984), and Gillespie et al. (1986). In the present study, the transformed channels were contrast stretched and arbitrarily assigned primary colors for display as a color composite image. The same method was used by Abrams et al. (1988) to map the lithology of Oman using enhanced Landsat Thematic Mapper data where they showed that the method could distinguish the spectral reflectance of different rock types and their weathering products. They stated further that the method produces images (R: 7; G: 5; B: 4) capable of recognizing variations among rock types. The method was also used by Rajendran et al. (2012) to discriminate ophiolite sequences of the Samail ophiolite. Rajendran and Nasir (2014) employed the method to discriminate limestone formations and associated lithologies in the Tanuf Valley and near the Sur region of parts of the Sultanate of Oman using ASTER spectral bands 8, 3, and 1. They demonstrated the capability of the method to map metamorphic rocks of the As Sifah region in Oman in 2015. In this study, The Landsat spectral bands ETM 7, 5 and 4 were used to delineate the marine terraces of the study region in the present study. A decorrelated RGB image (R: 7; G: 5; B: 4) of the region is shown in Fig. 8b.

We used Landsat decorrelated images to confirm the occurrence and spatial distribution of terraces discovered by field study and we were able to discriminate lithology and study the geomorphology of selected areas. This was supported by PCA image processing using ASTER data. The relationship between the spectral response of target minerals or rocks and numeric values extracted from the eigenvector matrix was used to calculate principal component (PC) images, which could determine which PC contained information about minerals and rocks, and whether the digital numbers (DNs) of pixels containing the target minerals and rocks had high (bright) or low (dark) values (Rajendran and Nasir, 2015; Rajendran et al., 2012, 2011; Crósta and Filho, 2003; Rokos et al., 2000; Loughlin, 1991; Crósta and Moore, 1990). The pre-treatment and processing of ASTER spectral bands for this technique were followed as described in Amer et al. (2010) and Abdeen et al. (2001). It is generally accepted that the first three high order principal components 1, 2, and 3 of PCA contain over 99% of the spectral information; hence these have been widely used for lithological mapping in preference to the subsequent low order principal components 4 and 5 which usually contain less than 1% of spectral information and have low signal-to-noise ratios. However, some of the higher order principal components provide subtle information about the presence of minerals and rock types that are spatially dominant in the image. Since the study region consists of marls that contain hydroxyl bearing aluminosilicate minerals that cause significant absorption in ASTER bands 4, 5 and 6, and limestones containing carbonate minerals that have absorptions in ASTER band 8, ASTER SWIR bands were chosen for PCA analysis (c.f. Richards and Jia, 1999) to discriminate the rocks of the region. Study of bright reflection and dark absorption of individual component of PCA of the study region (Rajendran et al., 2014, 2012, 2011) persuaded us

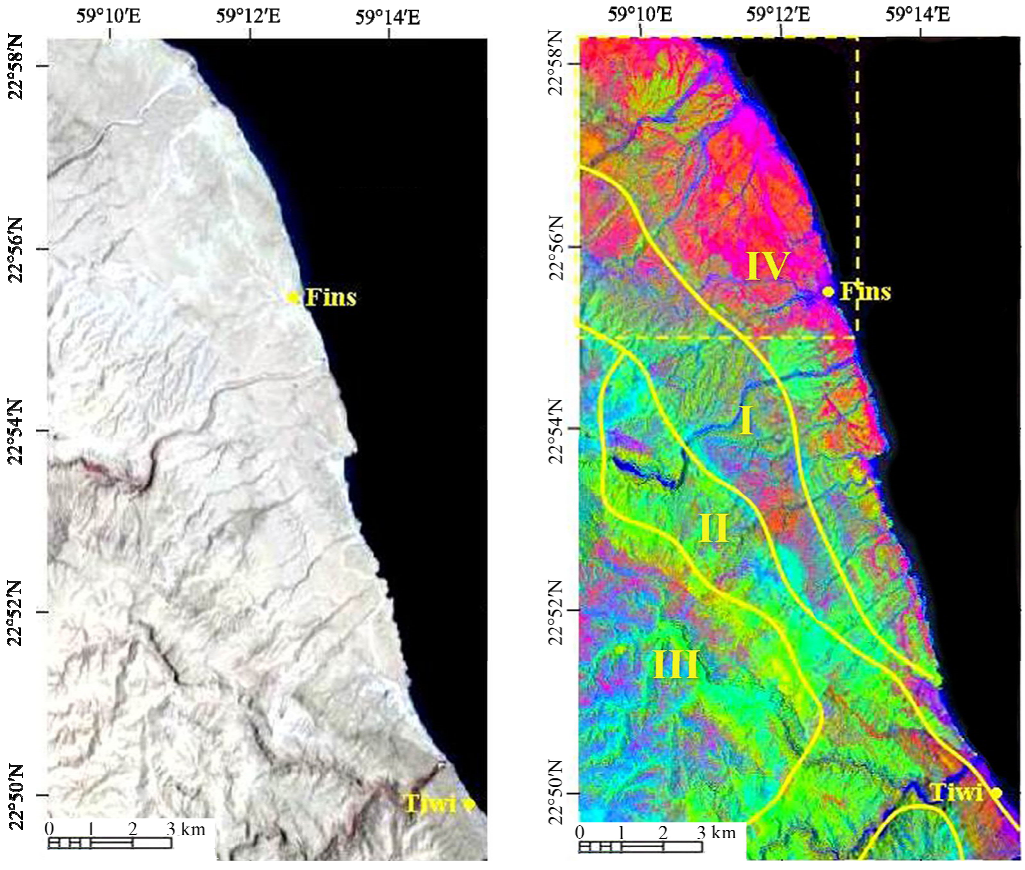

Figure 8. (a) Landsat RGB (4, 3, 2) image and (b) a de-correlated Landsat bands (7, 5, 4) image showing the distribution of terraces IV (Pliocene–Quaternary) and I, II and III (Tertiary) in and around the Tiwi and Fins region. The dashed box in (b) is the region chosen for ASTER image analyses for larger scale study.

to choose the principal components PC5, PC2 and PC1 (Fig. 9) to discriminate the different marine deposits and terraces of the study region. An RGB image using the principal components R: PC5, G: PC2, B: PC1 is given in Fig. 9 for discussion in the following section. The discrimination of rock types was further confirmed by mapping minerals of the region using a supervised classification method called spectral angle mapper (SAM) (Rajendran and Nasir, 2015, 2014; Rajendran et al., 2013; Hecker et al., 2008; Khan et al., 2007; Khan and Glenn, 2006; Rowan et al., 2003). This method encompasses hyperspectral tools such as minimum noise fraction (MNF) transformation, pixel purity index (PPI) and *n*-dimensional visualization, and classifies minerals based on collection of end-member spectral information (Rajendran and Nasir, 2015, 2014; Rajendran et al., 2013; Gabr et al., 2010; Kruse et al., 2003).

2.4 Regional Study of Terraces

Quantitative description of topographic profiles measured from digital elevation models (ASTER DEMs; Fig. 6) helps to define the occurrence, spatial distribution, and slopes of such terraces and controlling factors such as erosion, deformation, and variations of base level. We found noticeable spatial variations over the area, which we interpreted using de-correlated Landsat data (Fig. 8). Four types of terraces, I, II, III and IV were identified based on the interpretation of images, elevation and lithology (see above). The image in Fig. 8 shows increasingly strong impact of Quaternary deformation towards the east. Terraces I, II, and III are elevated well above the highest Pliocene–Quaternary uplift of over 100 m, and this is attributed to differential motion on the WNW- and NNE-striking faults that cut the mountain front (Kusky et al., 2005). The inner edges of the terrace surfaces represent paleo-shorelines corresponding to the main eustatic high-stands (Kusky et al., 2005). Quaternary marine terraces and related paleo-shorelines are exposed only in uplifted regions. The Type IV terrace surface, well preserved along the present coast, dips seawards whereas the types I–III terraces dip landwards (Fig. 7) or are essentially horizontal (Kusky et al., 2005; Wyns et al., 1992).

Types II and III terraces are bounded by faults of the WNW striking set. Fig. 7 shows the uplifted geomorphological units in a DEM profile while the RGB (R: 4; G: 3; B: 2) Landsat image in Fig. 8a, show that the terraces have different image textures, e.g. the Type IV terrace has a fine texture with flat or gentle slopes, Types I and II exhibit a medium-rough textures with medium slopes, and Type III has coarse texture with steep slopes. The increase of slope could be investigated using images of drainage morphology (Fig. 8a). The Type II terrace is highly deformed and a drainage pattern is not well represented. A de-correlated image derived from Landsat ETM spectral bands 7, 5 and 4 (Fig. 8b) shows the distribution of terraces based on lithological variations. The spatial distribution of terraces were mapped using a decorrelation stretched digital image processing method that studied the spectral responses of carbonate minerals using Landsat spectral bands 7, 5, and 4. Band 7 especially corresponds to the presence of carbonate and hydroxyl bearing minerals in the limestone formations. Bands 4 and 5 represent the and slightly altered aluminosilicate rich minerals. The image displayed all terraces in different tones to enable types I, II, III and IV to be delineated. The Type IV terrace appears in a pink tone and is located near present day sea level. The Type III terrace is illustrated in a mixed cyan tone and occupies the maximum elevation, and the Types I and II in between are displayed in cyan and green and blue and green mixed tones.

Terrace 1 is the most deeply and extensively incised by recent wadis, and is interpreted as the oldest terrace, followed by terraces II and III. Terrace IV is of a different character, seaward dipping along the present coast within the range of Pliocene–Quaternary sea level fluctuations so it may have a different origin from terraces I, II and III.

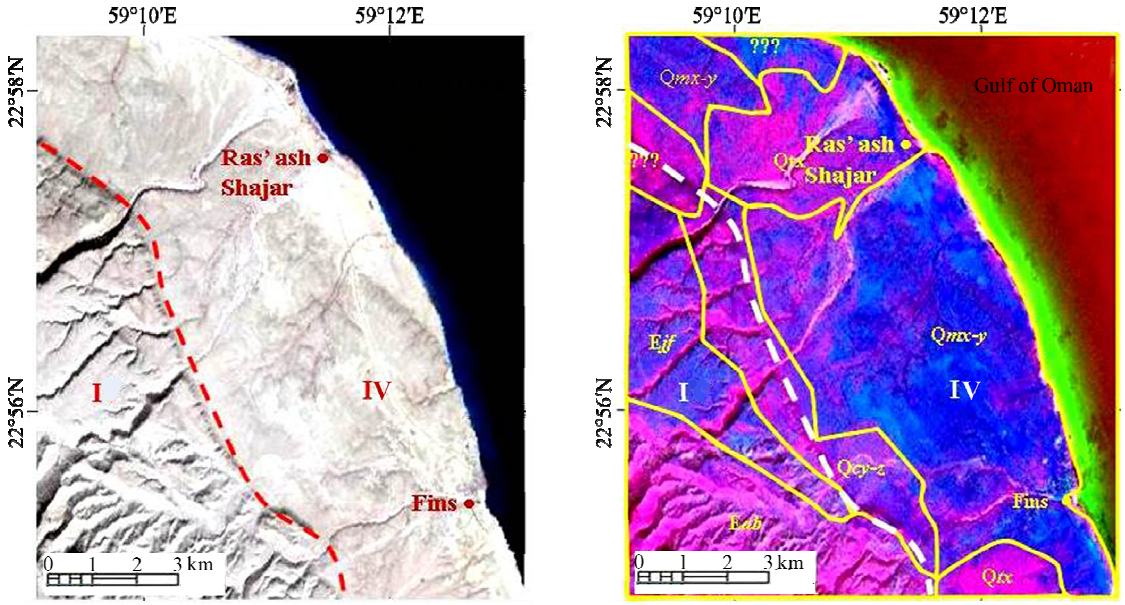

Figure 9. (a) ASTER RGB (3, 2, 1) image and (b) RGB image of PC bands (5, 2, 1) showing the distribution of terraces IV (Pliocene–Quaternary Age) and I (Tertiary Age) in and around Ra's ash Shajar and Fins region. See Fig. 3 for explanation of geological unit labels.

2.5 ASTER Application to Study of Marine Terraces

We present a detailed study of the terraces in the area between Ra's ash Shajar and Fins. The geology around the area is given in Fig. 3 and includes mainly sedimentary rocks of the Abat Formation (E*ab*) and Jafnayn Formation (E*jf*) of Late Paleocene–Early Eocene Age and ancient to sub-recent coastal deposits (Q*mx-y*) slope colluvium and scree (Q*cy-z*), ancient alluvial terraces (Q*tx*) and recent wadi alluvium (Q*tz)* of Quaternary Age. The Lower Tertiary formations are composed of grey to white marly limestones with chert nodules and the upper formations consist of massive bioclastic limestone and conglomerate. The formations are overlain by Quaternary deposits (Rajendran and Nasir, 2014). Figure 9a is an ASTER FCC image (R: 3; G: 2; B: 1) showing clearly the occurrence of terraces IV and III with different textures and variations in bright tones. The high resolution image shows clearly different drainage patterns which distinguish the different terrace surfaces. The terraces cap rock units with different lithologies (Figs. 4–5). The Type IV terraces have ancient and sub-recent coastal deposits and Terrace I consists of ancient alluvial terrace materials. This terrace is covered with recent wadi alluvium and slope scree.

The VNIR-SWIR spectral bands of ASTER were processed by the PCA method and the RGB image was processed using the principal components R: PC5, G: PC2, B: PC1, (Fig. 9b) clearly showing that the terraces are composed of carbonate materials which appear in pink and blue (Rajendran and Nasir, 2015, 2014). The terrace surfaces are exhibited in blue and the Abat Formation which consists of grey to white marl and micritic limestone with chert nodules appearing in pink on the image. Although all formations of the region are made of similar sedimentary rock materials (Fig. 3), textural differences were able to delineate the boundaries between terraces. Terrace IV has a smooth texture representing a smooth surface with little or no drainage patterns. In contrast, Terrace I exhibits a relatively coarse texture and has a well-developed incised drainage pattern. The increase of slope from east to west between the terraces can be understood as follows. The Type IV terrace surface is young and overlaps the Type I terrace, and thus is likely related to recent sea-level rise. The Type I terrace formed as a fluvial terrace because the terrace deposits consist of unsorted sub-angular gravel clasts like those observed in a modern riverbed. The Type I terrace consists of gravel with sand, sand with gravel, sandy silt, and soil. These finer sediments correspond to a paleosol containing granules of colluvium from the adjoining slope. The inner edges of the Type IV terrace could be clearly delineated. A light green tone represents the extrusion of fresh water along the coast (Kusky et al., 2005). The ASTER principal components image proved beneficial in the discrimination of the formations of the area.

2.6 Mineralogical Mapping

To support the above interpretation of the characteristics of the terraces, to delineate the occurrence of sedimentary formations of the region and to evaluate the capability of satellite sensors, mapping of minerals was performed using the ASTER VNIR-SWIR spectral bands by a spectral angle mapper (SAM) method. The method applied to the study area was initially determined by the inherent dimensionality of MNF image data which show an increase of noise from MNF bands 1–9 (Rajendran and Nasir, 2015, 2014; Rajendran et al., 2013). These bands were further processed to discover the most spectrally pure (extreme) pixels that contain mineral information of the image by PPI with a PPI iteration value of 10 000 (the maximum). The default threshold value was 2.5 and the SAM angle of 0.10 radians. The values set by the SAM procedure classified all the pixels (162 750 pixels in the total area 36.618 km^2 of the image). Figure 10 shows spectra (*n*-D class mean) derived based on end-members. Table 1 provides the number of pixels classified with their relative percentages and the total area of their distribution. Figure 11 is an SAM classified image and shows the occurrence and spatial distribution of minerals in the sedimentary formations of the study area with respective colors in the *n*-D class mean spectra. The SAM image can be compared with the geological map (Fig. 3) and the principal components image (Fig. 9b) discussed above. More details on the processing of image and absorption characters of *n*-D class mean spectra can be found in Rajendran and Nasir (2015, 2014), Rajendran et al. (2013), Gabr et al. (2010), Rowan and Mars (2003), and Kruse et al. (1993).

The SAM image (Fig. 11) shows the classified pixels in the six *n*-D classes viz.: *n*-D class #1, *n*-D class #3, *n*-D class #5, *n*-D class #7, *n*-D class #8 and *n*-D class #10 (Table 1; Figs. 10–11). The pixels of *n*-D class #2, *n*-D class #4, *n*-D class #6 and *n*-D class #9 do not show any significant mineral concentrations or distribution in the area (Figs. 10–11). The mean spectra of *n*-D class #1 show absorption around 0.7 μm and flat absorptions from 1.6–2.5 μm (Fig. 10). The absorption is due to presence of hydroxyl molecules (Rajendran and Nasir, 2015) in the sea water of the study area. About 7 458 red pixels (1.678 0 km^2) were classified and fresh water occurrences were studied in the field (Kusky et al., 2005). The occurrence and

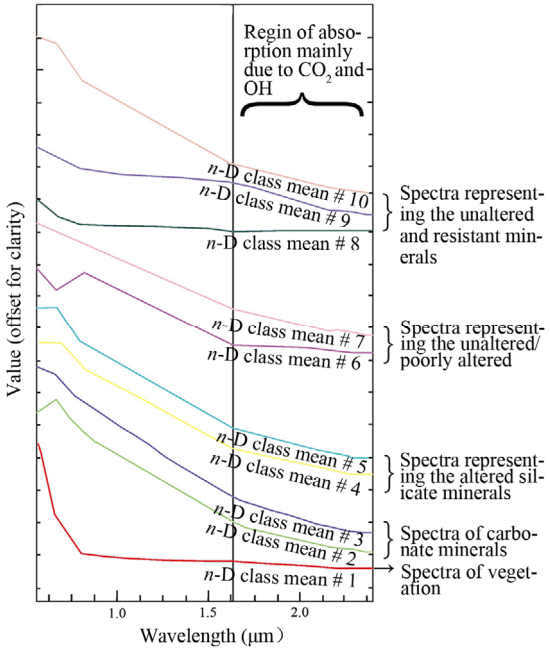

Figure 10. Plot of spectra (*n*-D class mean) derived, based on end-members.

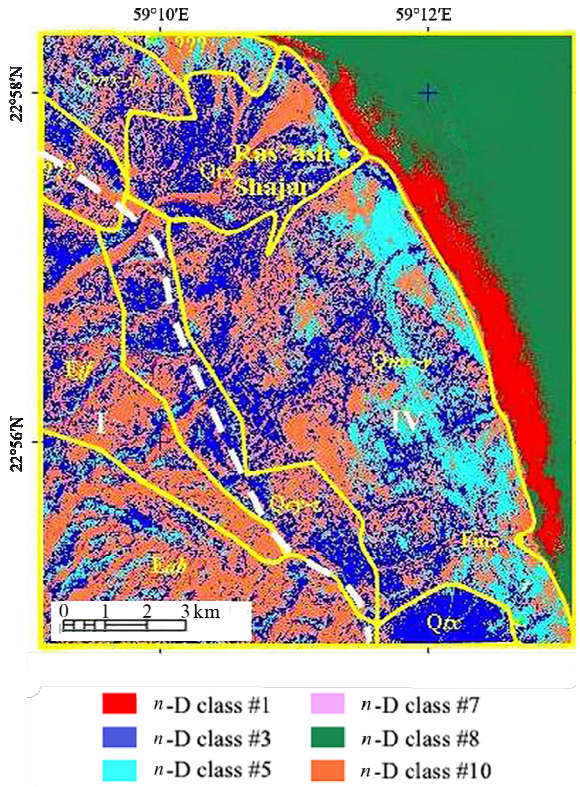

Figure 11. SAM image showing the minerals of formations in and around the Ra's ash Shajar and Fins region. See Fig. 3 for explanation of geological unit labels.

spatial distribution of dolomite was detected over about 10.102 7 km^2 shown in blue color by *n*-D class #3 (Rajendran and Nasir, 2015, 2014; Rajendran et al., 2013). The extracted end-member spectra of *n*-D class #3 show strong absorptions in the region of 1.6–2.5 μm due to the presence of CO_3. Blue pixels were observed in almost all of the sedimentary formations in the study area indicating that the area is covered by dolomite-bearing rocks. The minerals present in ancient alluvial fans and wadi alluvium are due to weathering, transportation and deposition of dolomite from Quaternary marine terraces. The image shows about 4.249 8 km^2 of occurrence and spatial distribution of OH-bearing alumino-silicate minerals such as amphibole, mica and chlorite groups in cyan color from *n*-D class #5. The alumino-silicate minerals were transported from marl deposits of the Abat Formation in the region. The absorption characters of OH and CO_3 bearing altered and carbonate rocks and minerals are described in Rajendran and Nasir (2015, 2014), Rajendran et al. (2014, 2013) and Abrams et al. (1988). Pixels of *n*-D class #7 (0.718 0 km^2 in maroon) cover the surfaces of Types I–III terraces composed of limestone, conglomerate, white and grey marl or micritic limestone of the Jafnayn and Abat formations. The distribution of pixels represents the presence of slightly altered alumino-silicate minerals distributed in eroded wadis and terraces. Pixels of *n*-D class #8 (6.120 4 km^2 in sea green) are represented by saline seawater of the Gulf of Oman. The spectra of the class show similarity to the spectra classified by fresh water molecules, the *n*-D class #1. The ASTER sensor is capable of diluted brackish sea water from saline sea water. The mean spectra of *n*-D class #10 appears in coral color (about 13.648 2 km^2) and shows the occurrence of unaltered and resistant silica and silicate minerals in the region. Such minerals are associated with the slightly altered minerals of *n*-D class #7 in the area (Rajendran et al., 2013).

Overall, the study of the SAM image confirms the occurrence of carbonate bearing sedimentary formations. The study indicates that: 1. the study area is mainly underlain by dolomite-bearing deposits; 2. the occurrence of OH bearing alumino silicate minerals in ancient and recent alluvial terraces and wadi alluviums of the Tertiary deposits; 3. the occurrence of unaltered resistant minerals on the terrace surfaces; and 4. the dilution of sea water by fresh water in the coastal region. The identification of different group of minerals within the marine deposits shows that SAM has potential to identify the minerals deposited in marine depositional environments. The study supports the interpretations of ASTER PCA image (Fig. 9b).

3 DISCUSSION AND SPECULATIONS ON THE SIGNIFICANCE OF THE RESULTS

Our studies have shown that the NE coast of Oman contains a series of erosional and depositional terraces that range in elevation from a few meters above modern sea level, to more than 1 km above sea level. We interpret these terraces as representing a complex interaction between sea level changes and uplift on a migrating flexural bulge related to the contemporary Arabia-Eurasia collision.

Terrace IV consists of a series of seaward-dipping subterraces, the most prominent of which are at 10–20 and 30–50 m above sea level, is Pliocene–Quaternary (Weichselian) in age and within the range of Pliocene–Quaternary sea level fluctuation. The lower levels (10–20 m) of this composite terrace represent a classical marine terrace related to sea level changes during the last glacial period. The origin of the 30–50 m steps on this composite terrace remains uncertain.

Terraces I, II, and III are above the range of sea level fluctuations. On geomorphological grounds, Terrace I appears to be older than Terrace II, which appears older than Terrace III. These terraces are horizontal or landward dipping, and are bounded by down-to-the-trench normal faults on the outer trench slope as the Arabian Platform is being subducted beneath the Makran accretionary wedge. We interpret these terraces as having formed on the outer slope of the migrating flexural bulge of the Arabian-Eurasian collision zone as it migrated across the Arabian Platform (Fig. 12). They have now passed over the crest of the bulge and are subsiding and will eventually sink beneath the Gulf of Oman as convergence continues, to ultimately disappear beneath the Makran.

Migration of flexural bulges through forelands in modern and ancient collision belts has been well-documented, one example being from the Ordovician Taconic orogen in North America (Bradley and Kusky, 1986). In that example, sediments of the eastern North American passive margin were uplifted several hundred meters as the bulge approached, rose out of the sea to become subaerially exposed, eroded to form erosional/depositional surfaces locally covered by basement-derived colluvium, then dropped down towards the trench on a system of listric normal faults (Bradley and Kusky, 1986), in a

manner analogous to the contemporary Arabia-Eurasia collision along the coast of Oman.

Further work is needed to determine the precise ages of terraces I, II, and III, and the ages and significance of the multiple steps in Terrace IV to test this scenario, perhaps using cosmogenic isotopic exposure ages. At current rates of plate motion (Fig. 12, Terraces I–III should be between 3.75 and 7.5 Ma old, with Terrace I older than II and in turn older than III.

4 CONCLUSIONS

We have used a combination of field studies, structural and stratigraphic analysis, combined with GIS and remote sensing technologies to document morphology, ages and histories of a series of Tertiary–Quaternary terraces on the northern Arabian Platform in Oman. These terraces are interpreted to have formed above the migrating flexural bulge in the foreland of the Arabian-Eurasian collision, as the Makran accretionary wedge loads the edge of the Arabian Platform. The terraces record a complex interaction between this tectonic uplift and eustatic sea level changes from the Pliocene through the last glacial period in the Weichselian. The interaction remains active to this day.

Multidisciplinary studies combining field geology, structural mapping, remote sensing, GIS, geomorphology and geochronology have great potential for unravelling past and present plate interactions and mitigating moderate sized earthquakes on the northern coast of Oman. Future work needs to use radiocarbon and cosmogenic isotopic surface exposure dating to verify the calculated ages of the older terraces related to flexural bulge migration through the Arabian Platform, and to further document the complex geomorphology and structure related to the actively migrating forebulge.

Table 1 Distribution of pixels of study area in the SAM *n*-D classes

n-D classes	No. of pixels	% in total area	Area in km²
n-D class mean #1	7 458	4.582	1.678 0
n-D class mean #2	20	0.012	0.004 5
n-D class mean #3	44 901	27.589	10.102 7
n-D class mean #4	178	0.109	0.040 0
n-D class mean #5	18 888	11.606	4.249 8
n-D class mean #6	45	0.028	0.010 1
n-D class mean #7	3 193	1.962	0.718 0
n-D class mean #8	27 202	16.714	6.120 4
n-D class mean #9	206	0.127	0.046 3
n-D class mean #10	60 659	37.271	13.648 2
Total	162 750	100.000	36.618 0

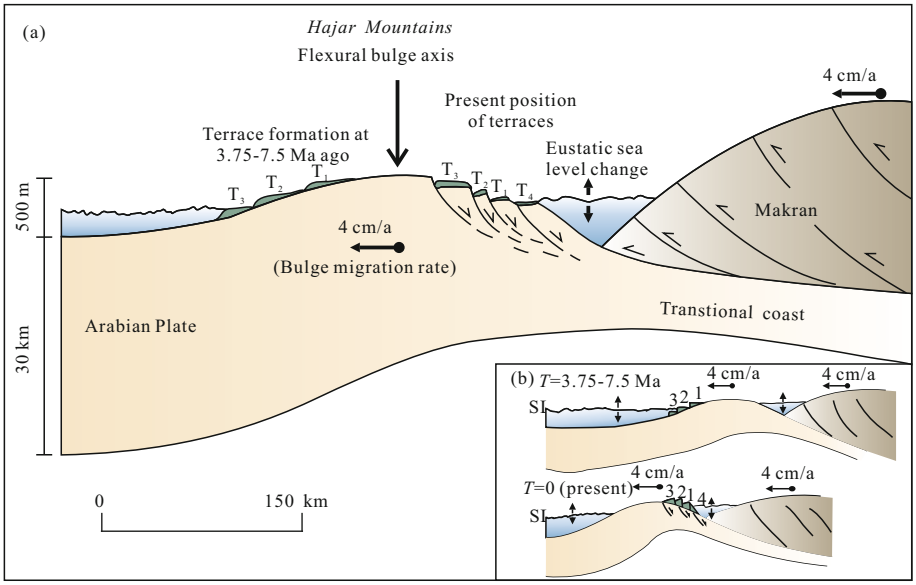

Figure 12. Speculative tectonic model for the origin of terraces and planation surfaces. (a) Diagram shows the model (with vertical exaggeration) where a flexural bulge related to the migrating load of the Makran accretionary wedge migrated across the Arabian margin at 3.75–7.5 Ma, uplifting terraces T_1–T_3 on the outer slope during a sea level high stand. As the bulge continued to migrate through the margin at 4 cm/a (the Arabian/Makran convergence rate), the uplifted terraces passed over the axis of the bulge to their present position where they are subsiding, and sinking into the Gulf of Oman in the foredeep of the collision zone. Quaternary sea level rise has added an additional terrace (the lower steps of T_4) that oversteps the older ones. Inset (b) shows the events in a 2-step time sequence. See text for additional discussion.

ACKNOWLEDGMENTS

The authors are thankful to NASA Land Processes Distributed Active Archive Center User Services, USGS Earth Resources Observation and Science (EROS) Center (https://LPDAAC.usgs.gov) for providing the ASTER data. The study was partially supported by Sultan Qaboos Internal (No. IG/SCI/ETHS/14/02), and by the National Natural Science Foundation of China (Nos. 91014002 and 40821061), and Ministry of Education of China (No. B07039), the Academic Innovation Base Plan of China University of Geosciences (Wuhan), and the 1 000 Talents Program, Central Organization Committee, China, awarded to Timothy M. Kusky. The final publication is available at Springer via http://dx.doi.org/10.1007/s12583-015-0656-2.

Open Access This article is distributed under the terms of the Creative Commons Attribution 4.0 International License (http://creativecommons.org/licenses/by/4.0/), which permits unrestricted use, distribution, and reproduction in any medium, provided you give appropriate credit to the original authors and the source, provide a link to the Creative Commons license, and indicate if changes were made.

REFERENCES CITED

Abdeen, M. M., Allison, T. K., Abdelsalam, M. G., et al., 2001. Application of ASTER Band Ratio Images for Geological Mapping in Arid Regions: The Neoproterozoic Allaqi Suture, Egypt. Proceedings of Geological Society of America Annual Meeting, Boylston. 33(6): 123

Abrams, M. J., Rothery, D. A., Pontual, A., 1988. Mapping in the Oman Ophiolite Using Enhanced Landsat Thematic Mapper Images. *Tectonophysics*, 151(1–4): 387–401. doi:10.1016/0040-1951(88)90254-5

Al-Lazki, A., Seber, D., Sandvol, E., et al., 2002. A Crustal Transect across the Oman Mountains on the Eastern Margin of Arabia. *Geoarabia*, 7(1): 47–78

Alsdorf, D. E., Smith, L. C., 1999. Interferometric SAR Observations of Ice Topography and Velocity Changes Related to the 1996 Gjálp Subglacial Eruption, Iceland. *International Journal of Remote Sensing*, 20(15–16): 3031–3050. doi:10.1080/014311699211606

Amer, R., Kusky, T. M., Ghulam, A., 2010. Lithological Mapping in the Central Eastern Desert of Egypt Using ASTER Data. *Journal of African Earth Sciences*, 56 (2–3): 75–82. doi:10.1016/j.jafrearsci.2009.06.004

Boote, D. R. D., Mou, D., Waite, R. I., 1990. Structural Evolution of the Suneinah Foreland, Central Oman Mountains. *Geological Society*, *London*, *Special Publications*, 49(1): 397–418. doi:10.1144/gsl.sp.1992.049.01.25

Bradley, D. C., Kusky, T. M., 1986. Geologic Methods of Estimating Convergence Rates during Arc-Continent Collision. *Journal of Geology*, 94(5): 667–681. doi:10.1086/629073

Chappell, J., Omura, A., Esat, T., et al., 1996. Reconciliation of Late Quaternary Sea Levels Derived from Coral Terraces at Huon Peninsula with Deep Sea Oxygen Isotope Records. *Earth and Planetary Science Letters*, 141(1): 227–236. doi:10.1016/0012-821x(96)00062-3

Crósta, A. P., Filho, C. R. D. S., 2003. Searching for Gold with ASTER. *Earth Observation Magazine*, 12 (5): 38–41

Crósta, A. P., Moore, M. J., 1990. Enhancement of Landsat Thematic Mapper Imagery for Residual Soil Mapping in SW Minas Gerais State Brazil—A Prospecting Case History in Greenstone Belt Terrain. Proceedings of Thematic Conference on Remote Sensing for Exploration Geology-Methods, Integration, Solutions, 7th, Calgary. 1173–1187

Deif, A., El-Hussain, I., Al-Jabri, K., et al., 2013. Deterministic Seismic Hazard Assessment for Sultanate of Oman. *Arabian Journal of Geosciences*, 6(12): 4947–4960

DeMets, C., Gordon, R. G., Argus, D. F., 2010. Geologically Current Plate Motions. *Geophysical Journal International*, 181(1): 1–80. doi:10.1111/j.1365-246x.2009.04491.x

Gabr, S., Ghulam, A., Kusky, T. M., 2010. Detecting Areas of High-Potential Gold Mineralization Using ASTER Data. *Ore Geological Reviews*, 38(1): 59–69. doi:10.1016/j.oregeorev.2010.05.007

Gardner, R. A. M., 1988. Aeolianites and Marine Deposits of the Wahiba Sands: Character and Paleoenvironments, *Journal of Oman Studies*, 3: 75–94

Gillespie, A. R., Kahle, A. B., Walker, R. E., 1986. Color Enhancement of Highly Correlated Images. I. Decorrelation and HSI Contrast Stretches. *Remote Sensing of Environment*, 20(3): 209–735

Glennie K. W., Boeuf, M. G. A., Hughes-Clarke, M. W., et al., 1973. Late Cretaceous Nappesin Oman Mountains and Their Geologic Evolution. *AAPG Bulletin*, 57(1): 5–27. doi:10.1306/819a4240-16c5-11d7-8645000102c1865d

Glennie, K. W., 2005. The Geology of the Oman Mountains: An Outline of Their Origin. Bucks: Scientific, Norwalk. 110

Glennie, K. W., Boeuf, M. G. A., Hughes-Clarke, M. W. M., et al., 1990. Inter-Relationship of Makran-Oman Mountains Belts of Convergence. *Geological Society Special Publications*, 49(1): 773–786. doi:10.1144/gsl.sp.1992.049.01.47

Haghipour, N., Burg, J. P., 2014. Geomorphological Analysis of the Drainage System on the Growing Makran Accretionary Wedge. *Geomorphology*, 209: 111–132. doi:10.1016/j.geomorph.2013.11.030

Hanna, S. S., 1986. The Alpine (Late Cretaceous and Tertiary) Tectonic Evolution of the Oman Mountains: A Thrust Tectonic Approach. Symposium on the Hydrocarbon Potential of Intense Thrust Zone, OAPEC, Kuwait. 2: 125–174

Hannss, C., Rähle, W., Kürschner, H., 1991. The Capital Area of North Oman: Basic Features of the Younger Caenozoic Relief Development on the Seaside of Central Oman. L. Reihert

Hecker, C. A., van der Meijde, M., van der Werff, H. M. A., et al., 2008. Assessing the Influence of Reference Spectra on Synthetic SAM Classification Results. *IEEE Transactins on Geoscience and Remote Sensing*, 46(12): 4162–4172. doi:10.1109/tgrs.2008.2001035

Khan, S. D., Glenn, N., 2006. New Strike Slip Faults and Litho-Units Mapped in Chitral (N. Pakistan) Using Field and ASTER Data Yield Regionally Significant Results.

International Journal of Remote Sensing, 27(20): 4495–4512. doi:10.1080/01431160600721830

Khan, S. D., Mahmood, K., Casey, J. F., 2007. Mapping of Muslim Bagh Ophiolite (Pakistan) Using New Remote Sensing and Field Data. *Journal of Asian Earth Sciences*, 30(2): 333–343. doi:10.1016/j.jseaes.2006.11.001

Kruse, F. A., Boardman, J. W., Hunnington, J. F., 2003. Comparison of Airborne Hyperspectral Data and EO-1 Hyperion for Mineral Mapping. *IEEE Transactins on Geoscience and Remote Sensing*, 41(6): 1388–1400. doi:10.1109/tgrs.2003.812908

Kruse, F. A., Lefkoff, A. B., Boardman, J. W., et al., 1993. The Spectral Image Processing System (SIPS)—Interactive Visualization and Analysis of Imaging Spectrometer Data. *Remote Sensing of Environment*, 44(2): 145–163. doi:10.1016/0034-4257(93)90013-n

Kusky, T. M., Ramadan, T., 2002. Structural Controls on Neoproterozoic Mineralization in the SE Desert, Egypt: An Integrated Field, Landsat TM, and SIR C/X SAR Approach. *Journal of African Earth Sciences*, 35(1): 107–121. doi:10.1016/s0899-5362(02)00029-5

Kusky, T. M., Robinson, C., El-Baz, F., 2005. Tertiary–Quaternary Faulting and Uplift in the Northern Oman Hajar Mountains. *Journal of the Geological Society*, *London*, 162(4): 871–888. doi:10.1144/0016-764904-122

Li, H., Huang, X. Y., Deng, Q. L., et al., 2012. Mapping of Planation Surfaces in the West Region of Hubei Province Using the DEM Painted Relief Model. In: Kusky, T. M., Xiang, W., eds., Bedrock Geology, Neotectonics, and Geological Hazards in the Three Gorges Area, China. *Journal of Earth Science*, 23(5): 719–730

Li, Z. Z., Wang, D. M., Liu, D. C., et al., 2015. Hyperspectral Remote Sensing Technology and Its Progress in Resources Exploration. *Earth Science—Journal of China University of Geosciences*, 40(8): 1287–1294

Loughlin, W. P., 1991. Principal Component Analysis for Alteration Mapping. *Photogrammetric Engineering and Remote Sensing*, 57(9): 1163–1169

Magilligan, F. J. B., Gomez, L. A. K., Mertes, L. C., et al., 2002. Geomorphic Effectiveness, Sandur Development, and the Pattern of Landscape Response during Jökulhlaups: Skeiðarársandur, Southeastern Iceland. *Geomorphology*, 44(1–2): 95–113. doi:10.1016/s0169-555x(01)00147-7

Mann, A., Hanna, S. S., Nolan, S. C., 1990. The Post-Campanian Tectonic Evolution of the Central Oman Mountains: Tertiary Extension of the Eastern Arabian Margin. *Geological Society*, *London*, *Special Publications*, 49(1): 549–563. doi:10.1144/gsl.sp.1992.049.01.33

Matthews, J. P., Jones, A. S., 1992. Mapping the Xigaze (Tibet) Ophiolite Complex with Landsat Thematic Mapper Data. *Journal of Himalayan Geology*, 3: 97–101

Philip, G., Ravindran, K. V., Mathew, J., 2003. Mapping the Nidar Ophiolite Complex of the Indus Suture Zone, Northwestern-Trans Himalaya Using IRS-1C/1D Data. *International Journal of Remote Sensing*, 24(24): 4979–4994

Rajendran, S., Al-Khirbash, S., Pracejus, B., et al., 2012. ASTER Detection of Chromite Bearing Mineralized Zones in Samail Ophiolite Massifs of the Northern Oman Mountain: Exploration Strategy. *Ore Geological Reviews*, 44(2): 121–135

Rajendran, S., Hersi, O. S., Al-Harthy, A. R., et al., 2011. Capability of Advanced Spaceborne Thermal Emission and Reflection Radiometer (ASTER) on Discrimination of Carbonates and Associated Rocks and Mineral Identification of Eastern Mountain Region (Saih Hatat Window) of Sultanate of Oman. *Carbonates Evaporites*, 26(4): 351–364. doi:10.1007/s13146-011-0071-4

Rajendran, S., Nasir, S., 2013. ASTER Spectral Analysis of Ultramafic Lamprophyres (Carbonatites and Aillikites) within the Batain Nappe, Northeastern Margin of Oman—A Proposal Developed for Spectral Absorption. *International Journal of Remote Sensing*, 34(8): 2763–2795. doi:10.1080/01431161.2012.748941

Rajendran, S., Nasir, S., 2014. ASTER Spectral Sensitivity of Carbonate Rocks-Study in Sultanate of Oman. *Advances in Space Research*, 53(4): 656–673

Rajendran, S., Nasir, S., 2015. Mapping of High Pressure Metamorphics in the AsSifah Region, NE Oman Using ASTER Data. *Advances in Space Research*, 55(4): 1134–1157

Rajendran, S., Nasir, S., Kusky, T. M., et al., 2013. Detection of Hydrothermal Mineralized Zones Associated with Listwaenites Rocks in the Central Oman Using ASTER Data. *Ore Geological Reviews*, 53(8): 470–488. doi:10.1016/j.oregeorev.2013.02.008

Rajendran, S., Nasir, S., Kusky, T. M., et al., 2014. Remote Sensing Based Approach for Mapping of CO_2 Sequestered Regions in Samail Ophiolite Massifs of the Sultanate of Oman. *Earth-Science Reviews*, 135(4): 122–140. doi:10.1016/j.earscirev.2014.04.004

Ravaut, P., Bayer, R., Hassani, R., et al., 1997. Structure and Evolution of the Northern Oman Margin: Gravity and Seismic Constraints over the Zagros-Makran-Oman Collision Zone. *Tectonophysics*, 279(1–4): 253–280. doi:10.1016/s0040-1951(97)00125-x

Richards, J. A., 1993. Remote Sensing Digital Image Analysis: An Introduction. Springer-Verlag, Berlin. 340

Richards, J. A., Jia, X. P., 1999. Remote Sensing Digital Image Analysis, Third Ed. Springer, Berlin. 363

Robertson, A., 1987. The Transition from a Passive Margin to an Upper Cretaceous Foreland Basin Related to Ophiolite Emplacement in the Oman Mountains. *Geological Society of America Bulletin*, 99(5): 633–653

Robinson, C. A., El-Baz, F., Kusky, T. M., et al., 2007. Role of Fluvial and Structural Processes in the Formation of the Wahiba Sands, Oman: A Remote Sensing Perspective. *Journal of Arid Environments*, 69(4): 676–694. doi:10.1016/j.jaridenv.2006.11.015

Rokos, D., Argialas, D., Mavrantza, R., et al., 2000. Structural Mapping and Analysis for a Preliminary Investigation of Possible Gold Mineralization by Using Remote Sensing and Geochemical Techniques in a GIS Environment: Island of Lesvos, Hellas. *Natural Resources Research*, 9(4): 277–293

Rollinson, H. R., Searle, M. P., Abbasi, I. A., et al., 2014. Tectonic Evolution of the Oman Mountains. *Geological Society of London Special Publication*, 392(1): 1–7

Rothery, D. A., 1984. The Role of Landsat Multispectral Scanner (MSS) Imagery in Mapping the Oman Ophiolite. *Geological Society*, *London*, *Special Publications*, 13(1): 405–413. doi:10.1144/gsl.sp.1984.013.01.33

Rowan, L. C., Mars, J. C., 2003. Lithologic Mapping in the Mountain Pass Area, California Using Advanced Spaceborne Thermal Emission and Reflection Radiometer (ASTER) Data. *Remote Sensing of Environment*, 84(3): 350–366

Rowan, L., Hook, S. J., Abrams, M. J., et al., 2003. Mapping Hydrothermally Altered Rocks at Cuprite, Nevada, Using the Advanced Spaceborne Thermal Emission and Reflection Radiometer (ASTER), a New Satellite-Imaging System. *Economic Geology*, 98(5): 1019–1027

Siddall, M., Rohling, E. J., Almogi-Labin, A., et al., 2003. Sea-Level Fluctuations during the Last Glacial Cycle. *Nature*, 423(6942): 853–858

Stollhofen, H., Stanistreet, I. G., von Hagke, C., et al., 2014. Pliocene–Pleistocene Climate Change, Sea Level and Uplift History Recorded by the Horingbaai Fan-Delta, NW Namibia. *Sedimentary Geology*, 309(6): 15–32

Van den Berg, A., Segal, G., Yuen, D. A., 2015. SEPRAN: A Versatile Finite-Element Package for a Wide Variety of Problems in Geosciences. *Journal of Earth Science*, 26(1): 89–95

Whitney, B. B., Hengesh, J. V., 2015. Geomorphological Evidence for Late Quaternary Tectonic Deformation of the Cape Region, Coastal West Central Australia. *Geomorphology*, 84: 160–174

Williams, R. S., Hall, D. K., Sigurdsson, O., et al., 1997. Comparison of Satellite-Derived with Ground-Based Measurements of the Fluctuations of the Margins of Vatnajokull, Iceland, 1973–1992. *Annals of Glaciology*, 20(3):53–71

Wyns, R., Béchennec, F., Le Métour, J., et al., 1992. Geological Map of Sur, Sheet NF 40-08, Scale 1 : 250 000. Directorate General of Minerals, Ministry of Petroleum and Minerals, Muscat

Zha, F. L., Ma, M., Chen, S. B., et al., 2015. Remote Sensing Lithologic Classification of Multispectral Data Based on the Vegetation Inhibition Method in the Vegetation Coverage Area. *Earth Science—Journal of China University of Geosciences*, 40(8): 1403–1408